Int. J. Solids Structures Vol. 24, No. 12, pp. 1243–1266, 1988
Printed in Great Britain.

0020–7683/88 $3.00 + .00

EFFECT OF TARGET BENDING IN NORMAL IMPACT OF A FLAT-ENDED CYLINDRICAL PROJECTILE NEAR THE BALLISTIC LIMIT

S. T. JENQ† and W. GOLDSMITH
Department of Mechanical Engineering, University of California, Berkeley, CA 94720, U.S.A.

and

J. M. KELLY
Department of Civil Engineering, University of California, Berkeley, CA 94720, U.S.A.

(*Received* 19 *January* 1988; *in revised form* 27 *July* 1988)

Abstract—The current work is concerned with the normal impact of flat-nosed cylindrical projectiles striking at a velocity in the vicinity of the ballistic limit on metallic targets. The ratio of target thickness to striker diameter ranges from 1/4 to 1/2. The resulting penetration model extends existing theories to include the extensive deformation of the target resulting from the bending effect. The dynamic and static stress–strain relations of 2024-0 aluminum are obtained by means of the split-Hopkinson bar technique and an Instron machine, respectively. A series of tests with 0.8 mm diameter pre-drilled holes in each target is conducted to assess the relative effects of bending and shear on the plate deformation. A total of 20 shots are executed to examine the phenomenon of the plate response under impact loading. The 12.7 mm diameter hard-steel projectiles are fired with a pneumatic gun against 3.18, 4.76, and 6.35 mm aluminum targets at a velocity of up to 182 m s^{-1}. A dynamic plastic bending theory is proposed that will be superposed on the previously developed one-dimensional phenomenological penetration model of Liss *et al.* (*Int. J. Impact Engng* 1, 321–341 (1983)), to permit a more accurate prediction of target response. This phenomenological model is numerically analyzed and compared with the experimental findings and the two-dimensional Lagrangian computational codes Dyna2d and Autodyn using a Cray X/MP-48 and PC-AT, respectively. Excellent correspondence with data is obtained for the projectile exit velocity when a higher impact speed is employed. The final deformation field computed from the model is not limited to a narrow zone and shows good correlation with the experimental data, especially for thinner targets.

INTRODUCTION

Plate impact is a highly complex phenomenon which involves the effects of strain rate, hydrodynamic, elastic, viscous and plastic wave motions, thermal strain softening (adiabatic shear), fracture initiation and propagation, fracture surface sliding, crushing, shattering, and even erosion and impact explosion at very high velocities (Backman and Goldsmith, 1978). No single analytical model has thus far been constructed that is capable of predicting all features of the event and that incorporates all the mechanisms cited and perhaps others that might be significant, for all ranges of impact velocity, types of bullet motion and angles of incidence, and for the various materials that have been employed for both projectile and target.

This paper is concerned with the problem of normal impact on metallic targets with a thickness ranging from thin to intermediate relative to the diameter of a blunt-nosed cylindrical projectile striking at a velocity in the vicinity of the ballistic limit. This region is of special interest because, in addition to either perforation, embedment or ricochet of the striker, extensive deformations of the target are observed. Several previous investigations have proposed a number of phenomenological models (Beynet and Plunkett, 1971; Landkof and Goldsmith, 1985; Woodward, 1987; Shadbolt *et al.*, 1983) for this process. Most of these descriptions focus on plugging or shearing behavior of the target and consider only uniaxial wave effects in the projectile (with the exception of a recent paper by Ravid and Bodner (1983) who considered two-dimensional effects, and axisymmetric response of the target). A recent model by Liss *et al.* (1983a), concentrating on the normal impact of blunt

---

† Present address: Institute of Aeronautics and Astronautics, National Cheng-Kung University, Tainan, Taiwan 70000, R.O.C.

cylindrical elastic/plastic projectiles on metallic plates of intermediate thickness takes into account the lateral constraint of and simple transverse shear propagation in the target. The phenomenon is described by a series of regions with changing mass resulting from momentum transfer induced by shock waves. However, neither this nor other models accounted for the extensive target deformation due to bending when impact occurs at speeds near the ballistic limit.

In the present analysis, the target is divided into two regions.

(1) The primary impact zone (the area under the projectile).
(2) The secondary zone (the remainder of the target).

A dynamic plastic bending theory is proposed that will be superposed on the previously developed one-dimensional phenomenological penetration model of Liss *et al.* (1983a) to permit a more accurate prediction of target response. The results from this model are corroborated by computational results for the system, and checked against experimental data resulting from tests specifically conducted to elicit the contribution of bending to target response in the neighborhood of the ballistic limit. Excellent correspondence with experimentally determined exit velocities of the striker was noted at higher impact speeds. The predicted deformation zone is not limited to a narrow zone and shows good correlation with test results, especially for the thinner targets.

EXPERIMENTAL APPARATUS

The major components of the experimental system used are similar to those employed previously (Calder and Goldsmith, 1971; Liss and Goldsmith, 1984). A schematic of the experimental setup employed is shown in Fig. 1. A split-Hopkinson bar (Hauser, 1966) was also used to determine the compressive dynamic properties of the target under impact loading.

The facilities employed in the experiment involve the following components.

Pneumatic ballistic gun

A compressed gas gun is used to launch the projectile. The gun is equipped with a firing device, pressure gage, high pressure gas tank, and associated instrumentation. The

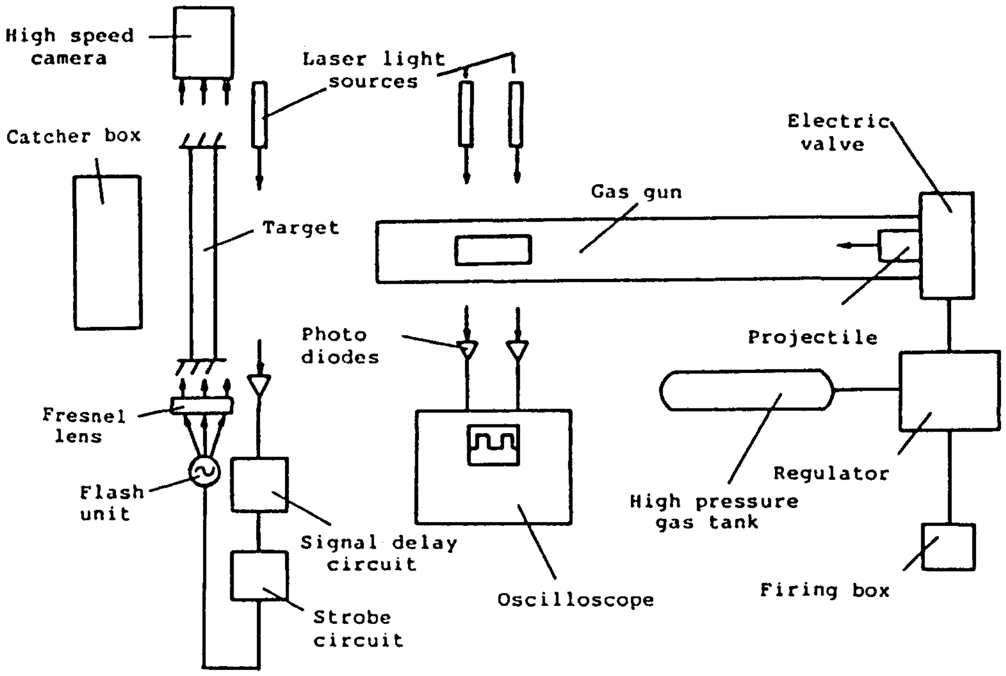

Fig. 1. Schematic of complete experimental setup.

gun has interchangeable barrels and is capable of propelling the 35.5 g, 12.7 mm diameter cylindrical steel projectile with a length of 38.1 mm at velocities up to 167 m s^{-1}.

Velocity measurement

Two Spectra-Physics (model 155) 0.5 mW helium–neon lasers are directed on parallel paths through two barrel slots near the muzzle end with an exact lateral spacing of 152 mm, and are focused on two photodiodes powered by a d.c. supply. A Hewlett-Packard Universal Counter Model 5325B or a Nicolet 4094 dual channel digital oscilloscope are used to record the signal, thus permitting the determination of the velocity of the striker. The error in this measurement is estimated to be less than 0.5% based on the rise time of the diode counter and the projectile geometry.

Framing camera

The advantage of using a framing camera is that one can view the entire penetration process and also be able to visualize the final motion of the plug and the projectile. In the current work, some of the tests are photographed using a Photec IV intermediate speed camera (Photonic Systems, Sunnyvale, California) lit by a circular array of eight 300 W bulbs or a Beckman–Whitley high speed camera. The framing rate of the Photec camera can be varied by indexing in the range from 100 to 10,000 s^{-1}. The Beckman–Whitley high speed camera uses a rotating prism and can achieve framing rates from 50,000 up to 1,000,000 s^{-1}. A 200 W flash unit and a stroboscopic circuit with a flash duration of approximately 1.8 ms are utilized to illuminate the whole penetration process. A capacitor bank of 100 μF with a power supply of 3600 V provides energy for another flash unit, but has the disadvantage of a shorter duration of the light pulse.

Target contour profilometer

This device consists of the track of a needle on the surface the contour of which is to be measured. Changes in elevation produce the deflection of a thin cantilever beam. Two pairs of resistance-type strain gages are mounted on opposite sides of the beam at the same distance from the support. The contact pin is mounted on the free end of the beam and adjusted so that the beam is always in a state of flexure over the entire domain of measurement. The deformed specimen is clamped on a movable table driven by a lead screw connected to an a.c. motor, with a stroke of 101.6 mm. The strain gage output is recorded on a Nicolet 4094 digital oscilloscope. This device is capable of measuring the transverse deformation of the final target profile up to about 17.8 mm with an accuracy of 5%.

Target and projectile material

Aluminum 2024-T6 sheet metal is machined to a circular shape, with a diameter of 140 mm and left in an oven for 2 h at a temperature ranging from 775 to 825°F. The material is then cooled in the oven at a rate of 50°F h^{-1} until the temperature reaches 500°F and then left in the oven to further cool slowly to room temperature. The thickness of the targets used are 3.18, 4.76, and 6.35 mm. The mechanical properties of the target material are shown in Table 1. The projectiles consist of flat-ended, 12.7 mm diameter oil-hardened drill rod with a length of 38.1 mm and a mass of 35.5 g, heat treated to a hardness of $60 \pm 2R_C$. In all tests, the targets were clamped in a rigid circular steel frame, as sketched in Fig. 1, which held the specimen over its entire circumference with eight 6.35 mm diameter bolts on the outer 12.7 mm. For some tests involving photography, a pair of steel clamps

Table 1. Mechanical properties of the target material (2024-0 aluminum)

Density, ρ	2700 kg m^{-3}
Poisson's ratio	0.33
Young's modulus, E	71.0 GPa
Static yield stress, S_y	75.8 MPa
Static ultimate stress, S_u	186.0 MPa
Brinell hardness	43–56 BHN

held the target at the top and bottom to provide a clearer view. In these cases, the clamping areas consisted of 12.7 mm wide 70° arcs, and five 6.35 mm diameter bolts in each clamp were used to hold the specimen in place.

Split-Hopkinson bar

The split-Hopkinson bar is used to investigate the dynamic properties of the 2024-0 aluminum used for the targets. The experiment is conducted by means of a striker bar, an input bar, a transmitting bar and a throw-off bar, all composed of 6.35 mm diameter titanium alloy Ti–6Al–4V, with a yield strength of 1.03 GPa. The input and transmitter bars are both 558.8 mm long. Two sets of Micro-Measurement 120 Ω, 3.18 mm gage length foil resistance strain gages, type EA-13-062AP-120 with attached leads, are mounted longitudinally on opposite ends of a diameter at a distance of 101.6 mm from the specimen end of the input and transmittal bars. The output signals of the strain gages are fed into the two active arms of a Wheatstone bridge to measure axial strains. The specimen is sandwiched between the input and transmitter bars and the contact surfaces are machined to be as close to plane and normal to the specimen axis as possible. Before the test, the bridge, with two active strain gages, is balanced by using potentiometers.

PENETRATION PLUGGING MODELLING

Earlier experimental results (Liss and Goldsmith, 1984) showed that plugging always occurs directly under the bullet when a blunt projectile strikes a metallic target of thin or intermediate thickness at normal incidence. A series of tests using a split-Hopkinson bar indicated that the 2024-0 aluminum target was relatively strain-rate insensitive over a range of rates from about 10 to 3000 s^{-1}. However, the stress levels were about twice that of their corresponding quasistatic values, as shown in Fig. 2. The present analytical model, modifed from Liss *et al.* (1983a) encompasses a series of rigid bodies the mass and velocity of which changes as the result of shock wave propagation.

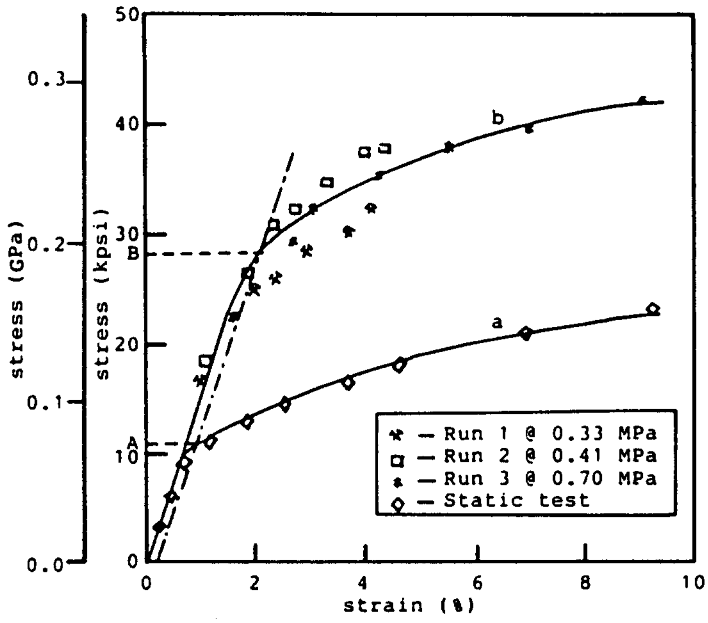

Curve		Point	
a	static curve	A	static yield stress
b	dynamic curve	B	dynamic yield stress (not constrained)

Fig. 2. Static and dynamic stress–strain curves for 2024-0 aluminum.

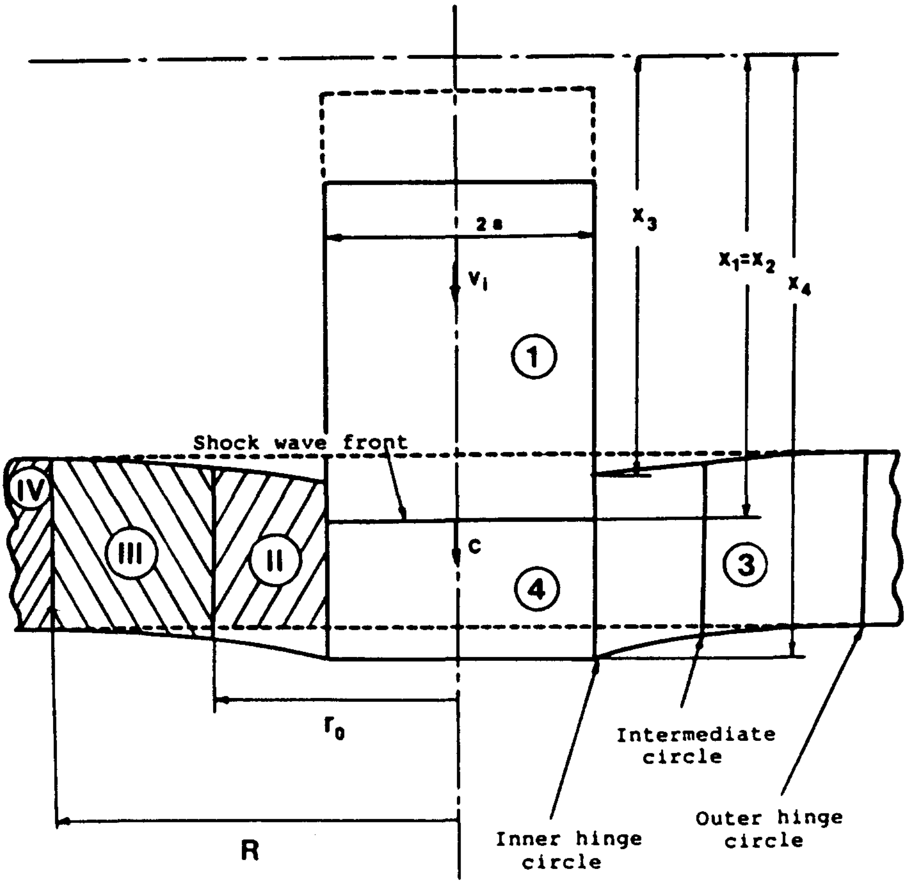

Fig. 3. Geometry of the projectile/plate system during the penetration process (erosion). Dotted lines represent the initial configuration.

In the current investigation, the projectile is made of hard steel and no permanent deformation was found after the tests. Therefore, the projectile is assumed to behave as a rigid body. The target shown schematically in Fig. 3 is at rest before the penetration process is initiated. It is divided into two regions.

(1) A primary impact zone (the area under the projectile, i.e. $r \leqslant a$).

(2) An exterior zone comprising the remainder of the target (i.e. $r > a$).

A deformable cylinder located in the primary impact zone will then be subjected to a thrust resulting from the propagation of one-dimensional uniform plane waves, generating coaxial shear at the periphery, and will also be constrained in any lateral flow by the surrounding material. The behavior of this local plugging phenomenon is characterized neither by a uniaxial stress wave motion nor by uniaxial strain wave motion, but rather by an intermediate effect, as described in Liss *et al.* (1983a). A brief summary of the events and the relevant equations developed there required for the present analysis are presented below.

Erosion

If the relative velocity of the projectile and the adjacent target material exceeds the plastic wave velocity of either the target or projectile, shock waves are emitted and propagated with this relative speed into the target or projectile, depending on the dynamic mechanical characteristics of the materials, and a shock wave front stands ahead of the interface. Material passing through the shock wave front melts and flashes, and cratering of the projectile or target material occurs. The system exhibits two rigid-body motions, composed of the projectile and target material ahead of the projectile (elements $\{1\}$ and $\{4\}$ as shown in Fig. 3). The results obtained by Liss *et al.* (1983a) determine the force applied to the projectile, which is the thrust of the shock layer opposing the projectile motion

$$F\langle t\rangle = M_1\frac{\mathrm{d}v_1}{\mathrm{d}t} = -A[Y_c+\rho_T(v_1-v_3)^2] \tag{1}$$

where M_1 and $V_1 = (\mathrm{d}x_1/\mathrm{d}t)$ are the mass and velocity of the projectile, i.e. element 1, respectively. Since the material in elements 3 and 4 is not exposed to the shock, $v_3 = v_4$ in this stage. The total force applied to the target during the first state is

$$F\langle t\rangle = \sigma_c A = [\rho_T(v_1-v_3)^2+Y_c]A \tag{2}$$

where ρ_1 is the density of the target and A the projectile cross-sectional area. Y_c is the dynamic target yield stress subject to a constraint resulting from the target material surrounding the region $r = a$. Further $v_i\langle t\rangle$ is the target particle velocity corresponding to element i.

Plastic wave propagation

Plastic wave propagation starts when the relative velocity between the projectile and the target material ahead of it is less than the plastic wave propagation speed. The total force exerted on target elements 3 and 4 during this stage is given by

$$F\langle t\rangle = [(v_1-v_4)^2\rho_T+Y_c]A+2\pi a\tau_s(x_2-x_1) \tag{3}$$

where τ_s is the dynamic shear stress at the periphery of element 2; during this stage, $v_3 = v_4$ and a is the radius of the projectile.

Plug separation

This begins when the plug is about to separate from the rear surface of the target. The total force applied to the target during the third stage is given as

$$F\langle t\rangle = [(v_1-v_3)(v_1-v_4)]A\rho_T+2\pi a\tau_s(H+x_3-x_1) \tag{4}$$

where H is the thickness of the target.

Plug slipping

This stage starts when the whole plug (elements 2 and 4) attains its final thickness and slips with uniform velocity equal to the projectile velocity. The stage is terminated when the projectile is not in contact with the target, that is, either perforation is completed or the projectile starts to rebound. The target material is assumed to be ductile enough so that the plug is nearly sheared out before final cracking has occurred. The force applied to the target during slipping is equal and opposite to the shear force exerted on the entire plug

$$F\langle t\rangle = 2\pi a\tau_s[H+x_3-x_1]. \tag{5}$$

Post-perforation deformation

Plug deformation after complete penetration is assumed to occur when the plug has been completely sheared out from the target, but before it acquires the projectile velocity. Erosion and shock wave propagation may occur successively. During this stage, there are no constraint effects to side flow or shear at the plug periphery and, therefore, the projectile does not exert any force on the target.

PLATE BENDING MODEL

The mechanism of the global target deformation due to impulsive loading treated here is bending, while membrane and transverse shear effects are not considered in this analysis. The fact that bending has a significant effect relative to shear in this velocity range is verified from experimental results for target plates pre-drilled with small holes and penetrated by projectiles, as is shown in the next section. In this analysis, the target is subjected to impulsive loading involving momentum transfer and dynamic shear forces occurring during the local plugging processes. The loading exerted on the target is determined from the penetration model described previously which results in a portion of the target deformation. The plate is modelled as infinite in its lateral extent and changes in target material properties, thermal and strain-rate effects (Valathur and Baker, 1971) associated with the deformation and fracture processes are not taken into account.

Elastic strains are considered to be small and are neglected compared to the plastic strains, so that the material behaves as a rigid body in the regions where no plastic deformation is produced. Since it is reasonable to represent the stress–strain relation for 2024-0 aluminum by a rigid/perfectly plastic model, the classical plate bending theory in conjunction with the rigid/perfectly plastic constitutive relation is adopted here to take into account the global target response when subjected to normal impact loading.

The perfectly plastic material considered here is assumed to obey the Tresca yield condition and its associated flow rules. For the case of plane stress, the yield condition is shown in Fig. 4. The hexagonal shape (ABCDEF) of this yield condition represents the loci of the pairs of principal values in terms of stresses σ_r and σ_θ or moments M_r and M_θ that cause plastic flow. All such points represent states of stress for which the maximum shearing stress is always $\sigma_0/2$, where σ_0 is the material dynamic yield stress. For the hexagon (ABCDEF) only the regimes ABC need to be investigated in the plastic analysis of this plate problem. As a continuation of the work of Shawa (1978), we divide the target into four regions by three concentric circles with the center at $r = 0$, associated with the regimes ABC of the Tresca yielding condition. One plastic hinge circle is always located at the edge of the impacting projectile, while a second circle is located where the normal shear force resultant is zero. There is a third circle, which is not a plastic hinge circle dictated by the Tresca yield condition, that is positioned between the two plastic hinge circles. The hinge circles associated with the kinematically admissible velocity fields then constitute the deformation pattern for the target. The detailed formulation is shown in the following paragraphs.

Consider the plastic bending of an initially stress-free circular plate under axisymmetric loading; the thickness H of the plate is constant and the plate has a mass μ per unit area. The z-axis of a cylindrical coordinate system (r, θ, z) is directed downwards. The target material is undeformed until the impact occurs, and the loading resulting from the process of contact is determined by the plugging model mentioned above. The kinematic formulation of the plate uses Kirchhoff's assumption. Therefore, the kinematic relations

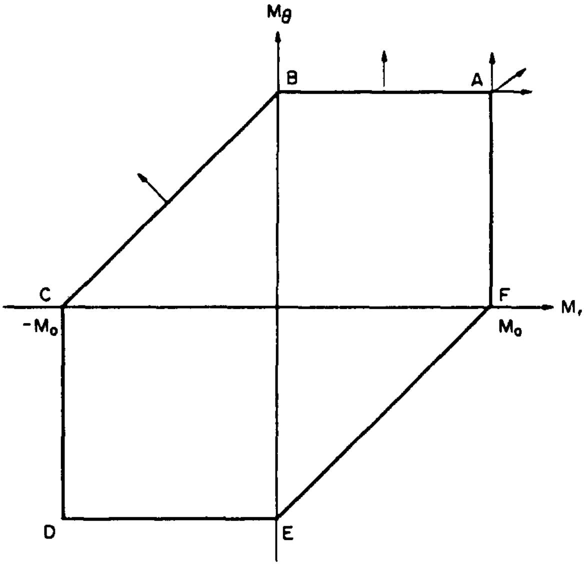

Fig. 4. Graphical representation of the Tresca yield condition.

between transverse displacement and the curvatures of the plate can be written as

$$K_r = -w_{,rr} \quad \text{and} \quad K_\theta = -\frac{w_{,r}}{r} \tag{6}$$

where K_r and K_θ are the curvatures with respect to the r- and θ-directions, and w refers to the transverse displacement of the plate. Note that $(\cdot)_{,r}$ represents the derivative of variable $(\cdot)$ with respect to variable r. The strains are determined by the relations

$$\varepsilon_r = zK_r \quad \text{and} \quad \varepsilon_\theta = zK_\theta. \tag{7}$$

Since the plate considered is of constant thickness, the plastic moments per unit circumferential length take the form

$$M_r = \sigma_r[H/2]^2 \quad \text{and} \quad M_\theta = \sigma_\theta[H/2]^2 \tag{8}$$

in the radial and circumferential directions, respectively. The dynamic equations result from the equilibrium relation or the minimum potential energy principle and, with μ as the mass per unit area, can be written as

$$(rQ_r)_{,r} + r[p - \mu w_{,tt}\langle r, t\rangle] = 0 \tag{9}$$

and

$$(rM_r)_{,r} - M_\theta - (rQ_r) = 0 \tag{10}$$

where $p\langle t\rangle = [F\langle t\rangle/(\pi a^2)]$ and $F\langle t\rangle$ and Q_r are the corresponding load and vertical shear force per unit length, respectively. The pressure p considered here is of such high intensity that the plate begins to yield instantaneously on impact.

As shown in Fig. 3, a hinge circle of radius a forms at the edge of the impact region. The region deformed by bending of the plates is confined within a hinge circle of radius R. In the following, we define the plate to be composed of four regions: region (I), $r \leqslant a$; region (II), $a < r \leqslant r_0$; region (III), $r_0 < r \leqslant R$; and region (IV), $r > R$. Regions (II) and (III) are designated to correspond to regimes AB and BC on the yield loci, based on the deformed pattern of the target observed from the experiments. An intermediate circle of radius r_0 such that $a < r_0 < R$ also forms, associated with point B of the Tresca yield hexagon.

Based on the flow rules associated with the yield conditions for the regions defined and the assumption of incompressibility, the admissible velocity fields of the target in terms of w and radial displacement u are as follows.

In region (I)

$$w\langle r, t\rangle = u\langle t\rangle; \quad w_{,t}\langle r, t\rangle = u_{,t}\langle t\rangle; \quad w_{,tt}\langle r, t\rangle = u_{,tt}\langle t\rangle. \tag{11}$$

In region (II)

$$\dot{K}_r = -w_{,rrt}\langle r, t\rangle = 0. \tag{12}$$

The velocity field in region (II) can be obtained after integrating eqn (12) twice with respect to the spatial variable r and the result is

$$w_{,t}\langle r, t\rangle = A\langle t\rangle + B\langle t\rangle r \tag{13}$$

where functions $A\langle t\rangle$ and $B\langle t\rangle$ are integration constants.

In region (III)

$$\dot{K}_\theta + \dot{K}_r = -\frac{1}{r}[rw_{,rt}\langle r, t\rangle]_{,r} = 0. \tag{14}$$

Here, the variable r is not equal to zero in the region considered. After integrating eqn (14) twice with respect to r and introducing the integration functions $C\langle t\rangle$ and $D\langle t\rangle$, we may obtain the corresponding velocity field as

$$w_{,t}\langle r,t\rangle = C\langle t\rangle \ln\langle r\rangle + D\langle t\rangle. \tag{15}$$

The integration functions will be determined from the appropriate boundary conditions and the continuity relations.

In region (IV)

$$w\langle r,t\rangle = w_{,t}\langle r,t\rangle = w_{,tt}\langle r,t\rangle = 0. \tag{16}$$

In this region, the material behaves as a rigid body. It should be recalled that, at the outer hinge circle, i.e. $r = R\langle t\rangle$, no deformation occurs and the material remains stationary. Application of the continuity condition to the location of the intermediate circle at $r = r_0\langle t\rangle$ results in the relations $w\langle r_0^-,t\rangle = w\langle r_0^+,t\rangle$, and the corresponding slope at $r = r_0$ of the plate is also continuous. Moreover, at the interface of regions (I) and (II), i.e. $r = a$, the velocity field is continuous and is equal to $u_{,t}\langle t\rangle$. Based on these conditions, all the parameters described in the velocity field have been determined as functions of time as well as the locations of the hinge circles and the intermediate circle. For convenience, the following non-dimensional variables are introduced:

$$\ddot{X}_1 = \frac{\mu a^2}{M_0} u_{,tt} \tag{17}$$

$$X_2 = \frac{a}{r_0\langle t\rangle} \tag{18}$$

$$X_3 = \frac{a}{R\langle t\rangle} \tag{19}$$

$$\psi = \ln\frac{r_0\langle t\rangle}{R\langle t\rangle} + X_2 - 1. \tag{20}$$

Hence, the velocity field obtained above can be rewritten in the non-dimensional form.

In region (I)

$$\dot{X}_1 = \frac{\mu a^2}{M_0} w_{1,t}\langle r,t\rangle. \tag{21}$$

In region (II)

$$\frac{\mu a^2}{M_0} w_{2,t}\langle r,t\rangle = \frac{\dot{X}_1}{\psi}\left[\ln\frac{X_3}{X_2} - 1 + \frac{r}{a}X_2\right]. \tag{22}$$

In region (III)

$$\frac{\mu a^2}{M_0} w_{3,t}\langle r,t\rangle = \frac{\dot{X}_1}{\psi}\left(\ln\frac{r}{a}\right)X_3. \tag{23}$$

Here w_1, w_2 and w_3 represent the transverse displacement corresponding to regions (I), (II), and (III), respectively. The acceleration field for the moving hinge solution can be obtained after taking the time derivative of the velocity components.

In region (I)

$$\frac{\mu a^2}{M_0} w_{1,tt}\langle r,t\rangle = \ddot{X}_1. \tag{24}$$

In region (II)

$$\frac{\mu a^2}{M_0} w_{2,tt}\langle r,t\rangle = \frac{\ddot{X}_1}{\psi}\left[\ln\frac{X_3}{X_2} - 1 + \frac{r}{a}X_2\right] + \frac{\dot{X}_1}{\psi}\left[\frac{r}{a}\dot{X}_2 + \frac{\dot{X}_3}{X_3} - \frac{\dot{X}_2}{X_2}\right]$$
$$-\frac{\dot{X}_1}{\psi^2}\left[\frac{r}{a}X_2 + \ln\left(\frac{X_3}{X_2}\right) - 1\right]\left[\dot{X}_2 + \frac{\dot{X}_3}{X_3} - \frac{\dot{X}_2}{X_2}\right]. \tag{25}$$

In region (III)

$$\frac{\mu a^2}{M_0} w_{3,tt}\langle r,t\rangle = \frac{\ddot{X}_1}{\psi}\ln\left(\frac{r}{a}X_3\right) - \frac{\dot{X}_1}{\psi^2}\left[\ln\frac{X_3}{(a/r)}\right]\left[\dot{X}_2 + \frac{\dot{X}_3}{X_3} - \frac{\dot{X}_2}{X_2}\right] + \left[\frac{\dot{X}_1}{\psi}\frac{\dot{X}_3}{X_3}\right]. \tag{26}$$

Hinges will propagate during the penetration process to dissipate the kinetic energy of the projectile.

The dynamic equations, eqns (9) and (10), are now applied to regions (I) and (II). Integrating this result with respect to r and keeping in mind that $M_\theta = M_0$ over this range, that $M_r = 0$ at $r = r_0$ and $M_r = M_0$ at the edge of the projectile $r = a$, there results

$$-\frac{12M_0}{a^2X_2} = \frac{M_0}{a^2}\ddot{X}_1\left\{6\left[\frac{1}{X_2} - 1\right] + \frac{1}{\psi}\left[-\frac{1}{X_2^3} + 3X_2 - 8 + \frac{6}{X_2} + \ln\frac{X_3}{X_2}\left(\frac{2}{X_2^3} - \frac{6}{X_2} + 4\right)\right]\right\}$$
$$+\frac{M_0}{a^2}\frac{\dot{X}_1}{\psi}\dot{X}_2\left\{\frac{1}{X_2}\left[-\frac{1}{X_2^3} + 3X_2 - 8 + \frac{6}{X_2}\right] + \frac{1}{\psi}\left\{\left(\frac{1}{X_2} - 1\right)\left[-\frac{1}{X_2^3}\right.\right.\right.$$
$$\left.\left.\left.+3X_2 - 8 + \frac{6}{X_2} + \ln\frac{X_3}{X_2}\left(\frac{2}{X_2^3} - \frac{6}{X_2} + 4\right)\right]\right\}\right\} + \frac{M_0}{a^2}\frac{\dot{X}_1}{\psi}\frac{\dot{X}_3}{X_3}\left\{\left(\frac{2}{X_2^3}\right.\right.$$
$$\left.\left.-\frac{6}{X_2} + 4\right) - \frac{1}{\psi}\left[-\frac{1}{X_2^3} + 3X_2 - 8 + \frac{6}{X_2} + \ln\frac{X_3}{X_2}\left(\frac{2}{X_2^3} - \frac{6}{X_2} + 4\right)\right]\right\}$$
$$+\left(\frac{1}{X_2} - 1\right)\left[\frac{-6F\langle t\rangle}{\pi a^2}\right] \tag{27}$$

where $F\langle t\rangle$ is the loading function and is computed from the phenomenological plugging model. Again, eqns (9) and (10) are applied to region (III), where $M_r - M_\theta = -M_0$. After integrating this result from $r = r_0$ to R and recalling that $M_r = M_0$ at $r = r_0$ and $M_r = -M_0$ at $r = R$, we obtain the second key moment equation

$$12M_0\left[2 - \ln\frac{X_2}{X_3}\right] = M_0\ddot{X}_1\left\{-\ln\frac{X_3}{X_2}\left\{6 + \frac{1}{\psi}\left[-\frac{2}{X_2^2} + 6 - 4X_2\right.\right.\right.$$
$$\left.\left.+\left(\frac{6}{X_2^2} - 6\right)\left(\ln\frac{X_3}{X_2}\right)\right]\right\} + \frac{1}{\psi}\left\{-\frac{3}{X_3^2} + \frac{3}{X_2^2} - \frac{3}{X_2^2}\ln\frac{X_3}{X_2} - \ln\frac{X_3}{X_2}\left(\frac{3}{X_2^2} - \frac{6}{X_2^2}\ln\frac{X_3}{X_2}\right)\right\}\right\}$$
$$+\frac{M_0\dot{X}_1\dot{X}_2}{\psi}\left\{-\ln\frac{X_3}{X_2}\left\{\frac{1}{X_2}\left[-\frac{2}{X_2^2} + 6 - 4X_2\right] + \frac{1}{\psi}\left(\frac{1}{X_2} - 1\right)\left[-\frac{2}{X_2^2}\right.\right.\right.$$
$$\left.\left.+6 - 4X + \left(\frac{6}{X_2^2} - 6\right)\left(\ln\frac{X_3}{X_2}\right)\right]\right\} + \frac{1}{\psi}\left(\frac{1}{X_2} - 1\right)\left[-\frac{3}{X_3^2} + \frac{3}{X_2^2}\right.$$

$$-\frac{3}{X_2^2}\ln\frac{X_3}{X_2}-\ln\frac{X_3}{X_2}\left\{\frac{3}{X_2^2}-\frac{6}{X_2^2}\ln\frac{X_3}{X_2}\right\}\Bigg]\Bigg\}+\frac{\dot{X}_1\dot{X}_3M_0}{\psi X_3}\left\{-\left(\ln\frac{X_3}{X_2}\right)\left(\frac{6}{X_2^2}-6\right)\right.$$

$$-\frac{1}{\psi}\left[-\frac{2}{X_2^2}+6-4X_2+\left(\frac{6}{X_2^2}-6\right)\left(\ln\frac{X_3}{X_2}\right)\right]+\frac{3}{X_3^2}+\frac{3}{X_2^2}-\frac{6}{X_2^2}\ln\frac{X_3}{X_2}$$

$$\left.-\frac{1}{\psi}\left[-\frac{3}{X_3^2}+\frac{3}{X_2^2}-\frac{3}{X_2^2}\ln\frac{X_3}{X_2}-\ln\frac{X_3}{X_2}\left(\frac{3}{X_2^2}-\frac{6}{X_2^2}\ln\frac{X_3}{X_2}\right)\right]\right\}-\frac{6F\langle t\rangle}{\pi}\ln\frac{X_2}{X_3}. \tag{28}$$

Now consider the requirement that the shear be continuous and, therefore, that the shear force should vanish at the outer hinge position, i.e. $Q_r = 0$, at $R\langle t\rangle$. This requirement may be written as

$$[rM_r]_{,r}-M_\theta=0=M_0\ddot{X}_1\left\{6+\frac{1}{\psi}\left[\left(-\frac{2}{X_2^2}+6-4X_2\right)\right.\right.$$

$$\left.\left.+\left(\frac{6}{X_2^2}-6\right)\ln\frac{X_3}{X_2}-\frac{3}{X_3^2}+\frac{3}{X_2^2}-\frac{6}{X_2^2}\ln\frac{X_3}{X_2}\right]\right\}+\frac{M_0\dot{X}_1\dot{X}_2}{\psi}\left\{\frac{1}{X_2}\left[-\frac{2}{X_2^2}+6-4X_2\right]\right.$$

$$\left.+\frac{1}{\psi}\left(\frac{1}{X_2}-1\right)\left[-\frac{2}{X_2^2}+6-4X_2+\left(\frac{6}{X_2^2}-6\right)\left(\ln\frac{X_3}{X_2}\right)-\frac{3}{X_3^2}+\frac{3}{X_2^2}-\frac{6}{X_2^2}\ln\frac{X_3}{X_2}\right]\right\}$$

$$+\frac{\dot{X}_1\dot{X}_3M_0}{\psi X_3}\left\{\left(\frac{6}{X_3^2}-6\right)-\frac{1}{\psi}\left[-\frac{2}{X_2^2}+6-4X_2+\left(\frac{6}{X_2^2}-6\right)\left(\ln\frac{X_3}{X_2}\right)\right.\right.$$

$$\left.\left.-\frac{3}{X_3^2}+\frac{3}{X_2^2}-\frac{6}{X_2^2}\ln\frac{X_3}{X_2}\right]\right\}-\frac{12F\langle t\rangle}{\pi}. \tag{29}$$

Equations (27)–(29) are three simultaneous relations the solution of which gives the global target response under this impact loading. These equations may be rewritten in matrix form as

$$[A][X]=[B] \tag{30}$$

where $[X]^T=[\ddot{X}_1,\dot{X}_2,\dot{X}_3]$ and the components of matrices $[A]$ and $[B]$ can be obtained from eqns (27)–(29). With the given initial conditions of the matrix and the loading conditions, the problem may be successively solved in time. The stationary hinge solution is applied to locate the initial hinges, i.e. r_0 and R at $t = 0$. This solution assumes that, at the instant of impact, the force exerted on the plate is constant. This initial hinge position can be obtained from the formulation described above with the assumption that, at this instant, the hinges are stationary. The plugging model of Liss *et al.* (1983a) is used to compute the corresponding penetration force, $F\langle t\rangle$, and the motion of the projectile and the plugging material at every time step. This interaction force is then used to compute the global target deformation described in this section based on the plate bending formulation. A computer program has been written to evaluate this penetration process by iteration.

RESULTS AND DISCUSSION

Bending and shearing angle measurement

In order to analyze the motion of the target subject to impact loading by a projectile, it is helpful to determine the major mechanism of the problem from a series of experiments. For a plate, the mechanisms for the global target response are usually dominated by a combination of membrane, bending, and shearing deformations in addition to plugging and/or petalling when penetration occurs. In the current investigations, the target thickness varies from 3.18 to 6.35 mm. Table 2 summarizes the initial conditions and the final

Table 2. Summary of impact tests

Run	Impact momentum (kg m s^{-1})	Projectile Impact velocity (m s^{-1})	Final velocity (m s^{-1})	Target Thickness (mm)	Target Maximum deflection (mm)†
1	2.74	77	0	3.2	13.2
2	3.053	86	0	3.2	18.2
3	3.30	93	0	3.2	20.2
4	3.8	107	0	3.2	15.2
5	5.325	150	127	3.2	14.9
6	6.8	172	157	3.2	9.3
7	4.108	104	0	6.4	12.6
8	4.86	123	0	6.4	14.4
9	4.98	126	—	6.4	13.4
10	6.926	150	110	6.4	13.9
11	13.66	343	300	6.4	8.0
12	16.43	416	382	6.4	7.6

† The maximum deflection used here is related to the value of x_i or $x_i + H$ for non-perforated or perforated tests, respectively.

deformations for the tests. A series of tests was conducted to examine the effects of bending and shearing on the target. Some targets were pre-drilled with a total of 20 holes (0.8 mm diameter) located along a radial line. Six tests were conducted with the impact velocity near the corresponding ballistic limit. A 0.8 mm diameter pin was inserted into these pre-drilled holes after the plates had been struck to measure the bending angles relative to the initial orientations with the aid of a comparator. The slopes of the corresponding deformed plate profiles were also derived from the measurement of the plate profile. The total slope is the sum of the shear deformation and bending deformation as in the analysis of a Timoshenko beam. Figure 5 shows that for thin plates (i.e. 3.18 mm thick), the effect of bending is dominant. The ratio of the shearing angle to the bending angle is approximately 30%. However, the shear effect is still important for the region next to the edge of the projectile. Figure 6 shows that the bending and the shearing effects are of equal importance for the 6.35 mm thick plates, since transverse shear becomes more significant as the thickness of the plate is increased.

Experimental results (Liss and Goldsmith, 1984) support the computed predictions that the extent of the zone of deformation beyond the contact region is limited to approximately a radius equal to that of the projectile for the thicker plates impacted at higher velocities. However, the comparison shows that the simple transverse shear mechanism does not account for the total target deflection when thin plates or those of intermediate thickness

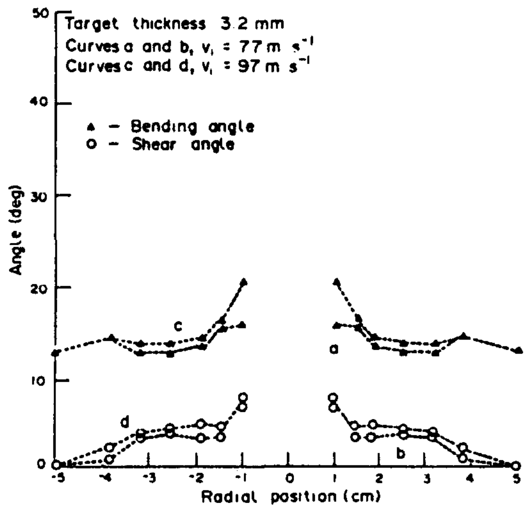

Fig. 5. Bending angle measurement. Target thickness, 3.18 mm.

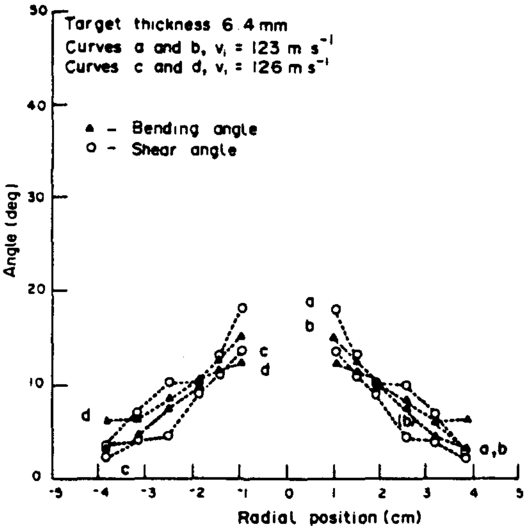

Fig. 6. Bending angle measurement. Target thickness, 6.35 mm.

are used. Moreover, the retention of a circular shape of the pre-drilled holes beyond a distance more than two projectile radii from the center indicates the absence of significant membrane effects in this region, although they are surely present in the region around the contact area.

Dynamic split-Hopkinson bar test

Three specimens made of a 2040-0 aluminum rod were examined dynamically. The output signals of two pairs of dual strain gages, located on the input and transmitter bars, respectively, are recorded. Curves a, b, and c, shown in Fig. 7, are plotted for strains of 1,

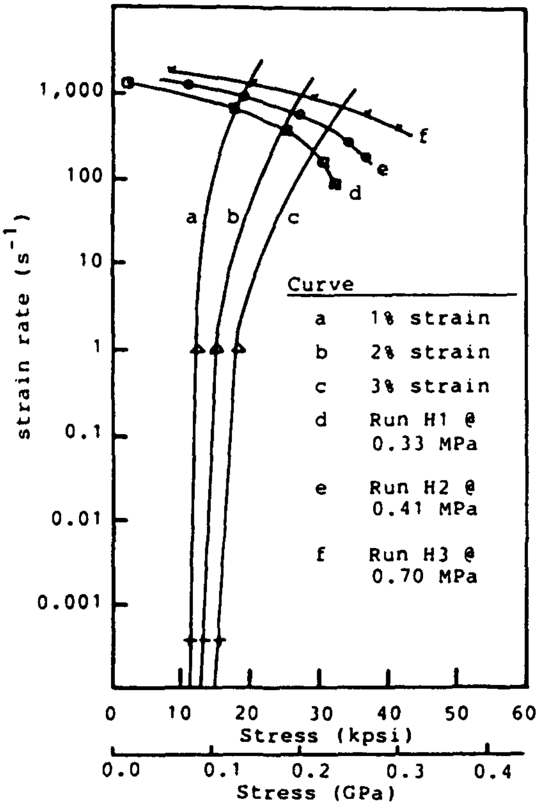

Fig. 7. Split-Hopkinson bar test for a 2024-0 aluminum rod.

Table 3. Summary of the maximum plate deflection and the projectile exit velocity from the bending and shear models

		Projectile Final velocity (m s^{-1})			Target Maximum deformation (x_1+H) at $r = a$ (cm)	
Run	Initial velocity (m s^{-1})	Bending model	Shear model	Thickness (mm)	Bending model (mm)	Shear model (mm)
R1	77	0	36.6	3.2	7.5 (7.8)†	4.96
R2	107	0	79.7	3.2	12.7 (13.2)	4.94
R3	160	121.6	105	3.2	14.0	3.67
R4	104	0	0	6.4	9.5 (11.5)†	7.63 (13.2)†
R5	150	107.5	106.5	6.4	7.7	7.3
R6	416	384.9	384.9	6.4	7.53	7.52

† The quantity in parentheses represents the maximum deformation at the center of the target, $r = 0$.

2, and 3%, respectively. The strain-rate effect of the 2024-0 aluminum material is not significant in comparison to materials such as mild steel, which was shown to be highly strain-rate dependent by Hauser (1966). The static and dynamic yield stresses, determined from an Instron machine and from a split-Hopkinson bar are 76 and 199 MPa, respectively. Since the effect of plug constraint on the dynamic yield stress in a plate differs from the unconstrained rod by a factor of nearly two as reported by Liss *et al.* (1983b) such a correction factor was applied to the uniaxial dynamic yield stress in the present analytical model.

Analytical model

The maximum plate deflections, x_1+H as shown in Fig. 8, at a distance equal to the projectile radius from the center of the target are obtained from the bending model and the previous shear model for various impact velocities near the ballistic limit. A summary of the computed results is shown in Table 3 for these two models. A set of experiments was also conducted to obtain the final target deformation contour by means of a profilometer. The test results were recorded using a Nicolet oscilloscope and its associated disk drive. Table 4 summarizes the experimental maximum deformations x_1+H of the target and the final projectile velocities of the rigid projectile for the present impact tests. The bending model predicts maximum target deformations that follow the same trend found in the experimental results. Figures 8(a)–(e) show the computed and measured target profiles after impact. The computed maximum plate deformation based on the bending model is closer to the test results than that based on Liss *et al.*'s shear model. For example, the maximum

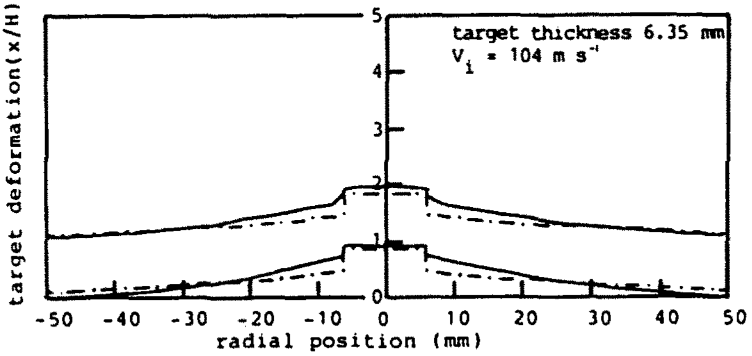

(a)

Fig. 8. Comparison of analytical and test results for the final target deformation of the bending model. Dotted and solid lines represent the computed and test results, respectively: (a) v_i = 104 m s^{-1}; (b) v_i = 150 m s^{-1}; (c) v_i = 77 m s^{-1}; (d) v_i = 107 m s^{-1}; (e) v_i = 150 m s^{-1}.

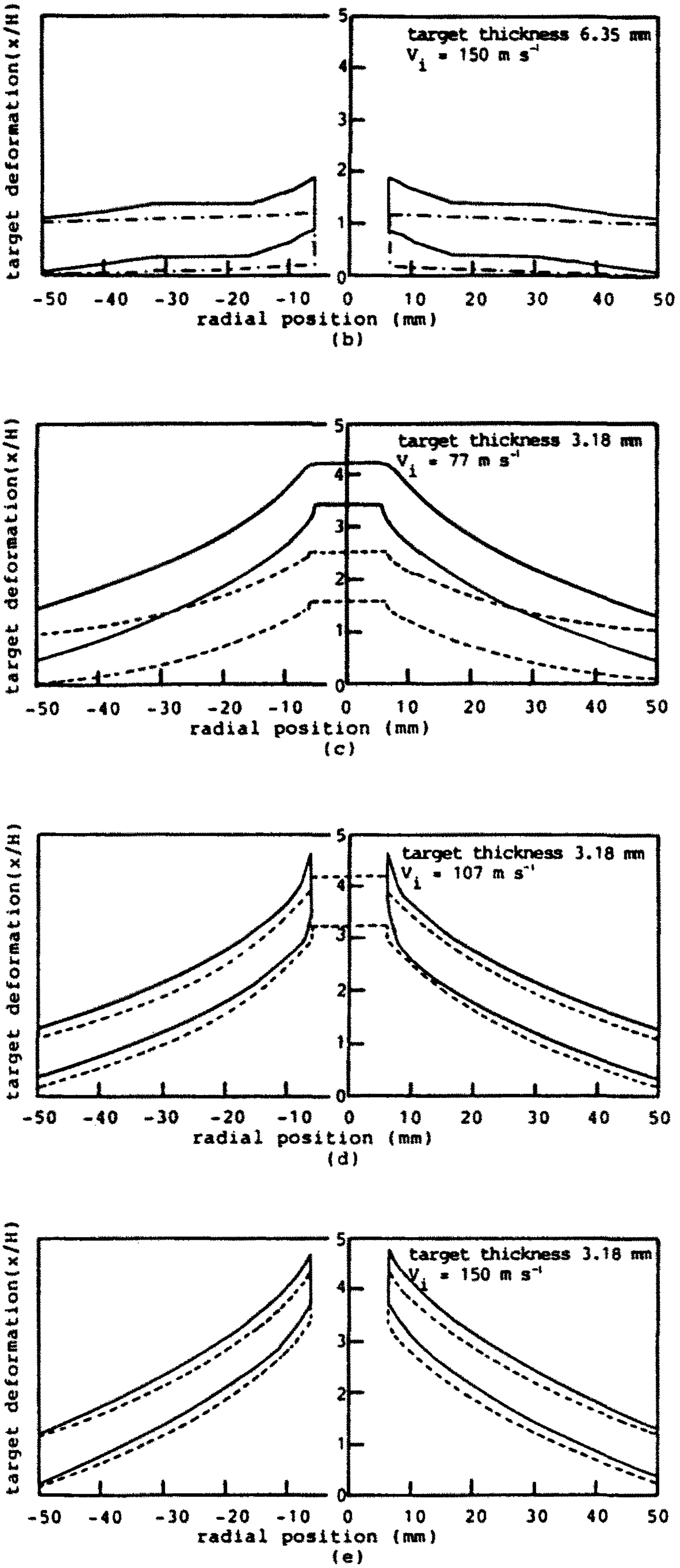

Fig. 8. (*Continued.*)

Table 4. Summary of the maximum plate deflection and the projectile exit velocity from Dyna2d and Autodyn codes

Run	Projectile Initial velocity ($m\ s^{-1}$)	 Final velocity ($m\ s^{-1}$)	Target Thickness (mm)	 Maximum deformation (x_3+H) at $r = a$ (mm)
D1	104	0	6.4	15.0†
D2	104	0	6.4	11.4†
A1	77	0	3.2	17.3†
A3	150	124	3.2	14.9
A4	104	0	6.4	17.2†
A5	150	120	6.4	12.0

†The quantity represents the maximum deformation at the center of the target, i.e. $r = 0$.

deformations obtained from the bending and this shearing model for a target 3.18 mm thick struck by a projectile with an initial velocity of 107 $m\ s^{-1}$ were 12.7 and 4.94 mm, respectively. These two predicted values differ from the experimental results by 18 and 67%. This shows that the dominant mechanism of thin target deformation subjected to impact loading is bending in comparison to shearing.

However, the transverse shear mechanism became important when the target thickness was increased. For example, the maximum deformation of a target 6.35 mm thick struck by a projectile travelling with an initial velocity of 150 $m\ s^{-1}$ is computed to be 7.7 and 7.3 mm for the bending model and the shear model, respectively. The corresponding differences between the predictions of these two models and test data are 45 and 48%. Results computed from the phenomenological model shown in Table 3 agree with the experimental findings.

(1) The maximum plate deflection for a specific target thickness increases as the projectile impact velocity is increased up to the ballistic limit.

(2) Beyond the ballistic limit, the gross plate deformation diminishes with increasing impact momentum.

(3) Transverse shear deformation is observed to be more affected near the zone $r \leqslant 3a$, where a is the projectile radius, especially for those cases where the plate is perforated.

The calculated target deformations obtained from the bending model and test results are shown in Figs 8(a) and (b) for a target thickness of 6.35 mm struck by the projectile at velocities of 104 and 150 $m\ s^{-1}$, respectively. Figures 8(c)–(e) present the experimental and computed results for the 3.18 mm thick target struck by a projectile at velocities of 77, 107 and 150 $m\ s^{-1}$, respectively. These diagrams show that the predicted target deformation is not restricted to the zone close to the projectile radius as indicated by the shear model, and the calculated final plate deformations resemble more closely the experimental findings. Nevertheless, the solutions still underestimate the target response compared to the tests. This may be due to the following reasons.

(1) The geometry of the plate is assumed to be infinite in the radial direction. As the plastic hinges propagate further away, more energy is required to accelerate the plate.

(2) In the simulation, we assume that the plate yield stress takes on the dynamic yield stress value. This may make the plate too stiff so that it differs from the actual material behavior during penetration.

(3) The phenomenological model assumes that the material properties do not vary during the penetration processes; however, the effect of plate softening and fracture phenomena may be significant.

Figure 9 shows the transverse deflection as a function of the radial position of a plate at various instants when struck at an initial velocity of 73 $m\ s^{-1}$ by a rigid blunt cylinder with a mass of 47 g and a diameter of 12.3 mm. The experimental findings of the plate deflection and the membrane solutions by Beynet and Plunkett (1971) and the solutions without inclusion of plugging are shown as the dashed line in the same plots at various

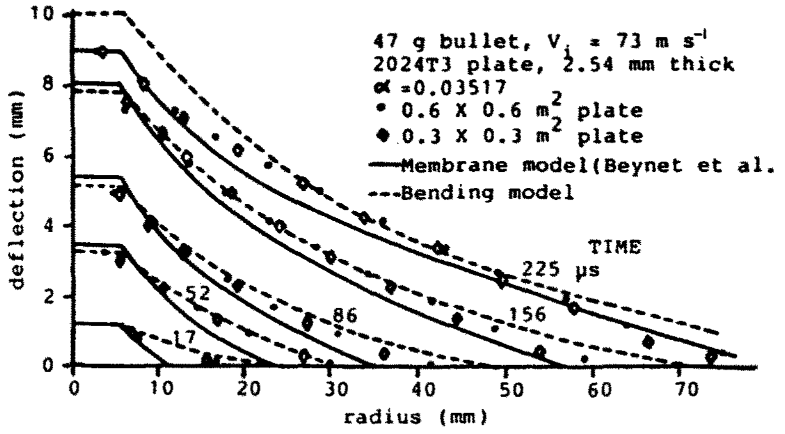

Fig. 9. Target plate response using the bending model without employing the plugging model, plotted at various times throughout the penetration process. The experimental data and the Beynet membrane solution are also shown.

instants. The results indicate that the bending solutions accurately predict the experimental findings. For this run, a static yield stress of the 2024-T3 aluminum plate was chosen as 0.345 GPa so as to correspond to the values used by Beynet and Plunkett (1971), while the dynamic yield stress was used for the present plate model. The plugging model is not incorporated here; the projectile is assumed to decelerate after impact and to move together with the target, and the target is assumed to be intact at all times.

The terminal projectile momentum is a useful and relatively easily measured variable. It can be employed to compare the predictions of the analytical model and the results of the tests. Figures 10(a) and (b) show the final projectile momentum as a function of the initial momentum for two different 2024-0 aluminum plate thicknesses, 3.18 and 6.35 mm. Predictions of the bending model and shear model are presented along with the experimental results. The computed final velocity for both models is shown in Table 3. The corresponding experimental data are presented in Table 2. Figure 10 shows that the theoretical curves generally follow the data quite well. Better agreement is obtained for the higher impact velocities; however, for impact velocities near the ballistic limit, the current model seems to predict a higher ballistic limit than the shear model. The flexural resistance of the plate is thus greater than that of shear for the present impact parameters.

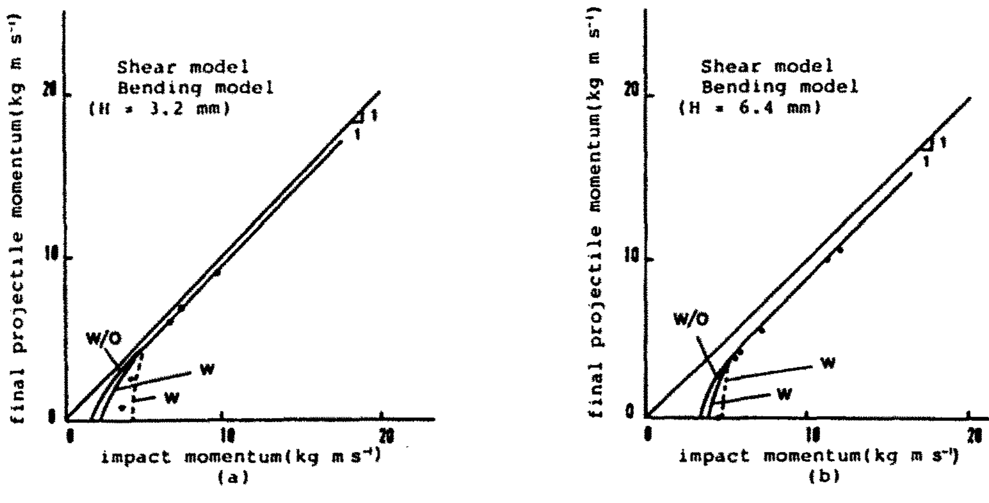

(a)

(b)

Fig. 10. Theoretical prediction of the final projectile momentum of the shear and bending models, and experimental results (○) as a function of initial momentum: (a) $H = 3.2$ mm; (b) $H = 6.4$ mm. w denotes inclusion of plugging; w/o represents the computation without the plugging mechanisms.

The strong transverse shear interaction in the plate bending problem can be treated by utilizing the Mindlin–Uflyand approach (Mindlin, 1951; Uflyand, 1948). The value of the shear correction factor depends on the assumptions employed and, in any event, is difficult to obtain numerically by a plate formulation. In order to investigate the effect of transverse shear, available codes such as Dyna2d and Autodyn are utilized here. The formulation of the code is based on continuum mechanics in conjunction with finite element or finite difference techniques to obtain an exact solution within the limits of truncation and round-off error. The effect of transverse shear is incorporated in these codes.

Lagrangian finite element code: Dyna2d

A Lagrangian finite element code, Dyna2d (Hallquist, 1978), is used to simulate the penetration process for a 2024-0 aluminum target of 6.35 mm thickness struck by a blunt rigid cylindrical projectile with an initial velocity of 104 m s^{-1}. These computations, which are based on a continuum mechanics formulation, incorporate all relevant plate deformation mechanisms and thus provide a measure of the effectiveness of the present plate mode which incorporates only a limited number of these behavior patterns. The simulations were performed on a Cray computer. The constitutive assumption used for the target is an isotropic linear work-hardening model. The projectile is assumed to be rigid with no permanent deformation allowed. Two cases involving this phenomenon, labelled D1 and D2 were computed. The difference between them is that Run D1 uses the static stress–strain data shown in Table 1, while Run D2 utilizes the dynamic stress–strain relation based on the following information proposed by Recht and Ipson (1963): yield stress σ_y (in MPa) = 3.92 BHN, and btan = 4.55 BHN, where BHN and btan represent the Brinell hardness number and the hardening parameter, respectively. The yield strengths for Runs D1 and D2 are 76 and 199 MPa, respectively. Plots of the simulations are shown in Figs 11(a) and (b) where the projectile has rebounded in the second diagram. Corresponding effective plastic strain contours were also obtained but are not shown here. The results indicate that the maximum deformation occurs at the center of the target with values of 15 and 11.4 mm for Runs D1 and D2, respectively. The maximum deformation for Run D1 is 19% larger than the experimental data due to the use of a static stress–strain data in this computation. Run D2 was corrected by using the dynamic stress–strain relationship and the results showed that the maximum deflection at the plate center underestimated the experimental results by 10%.

Lagrangian finite difference code: Autodyn

Two penetration problems were examined in the previous section using the program Dyna2d. However, the current version of Dyna2d does not have the capability to introduce new slide lines during computations. This is the key to properly solving the perforation problem using currently available codes. Therefore, Autodyn is employed to solve the case of 6.35 and 3.18 mm 2024-0 aluminum targets struck by a 35.5 g cylindrical, blunt steel projectile of 12.7 mm diameter. Several runs indicated by the letter A were performed; the material properties used are shown in Table 1. A summary of results is presented in Table 4. The important features of this code are given below.

(1) Interactive rezoning, which eliminates severe mesh distortions that occur when the target is subjected to high loading rates, such as occur in an impact.

(2) Editing impact/slide interfaces, which allows adding or deleting sliding lines during computation in order to simulate the fragmentation or fracture phenomenon occurring in the problem.

Figures 12(a) and (b) show the deformation field of a 6.35 mm target at a time 59 and 84 μs after impact is initiated. A slide line is generated that is located at the edge of the plug in the target and the projectile starts to push it out of the target, eventually resulting in perforation. The computed maximum deformation of the target after perforation was 12 mm, while the maximum deformation obtained from the test was 13.9 mm. These values differ by less than 14%. Figure 13 shows the evolution of the particle velocity of the projectile. The projectile exit velocity is computed to be around 120 m s^{-1}, while the exit

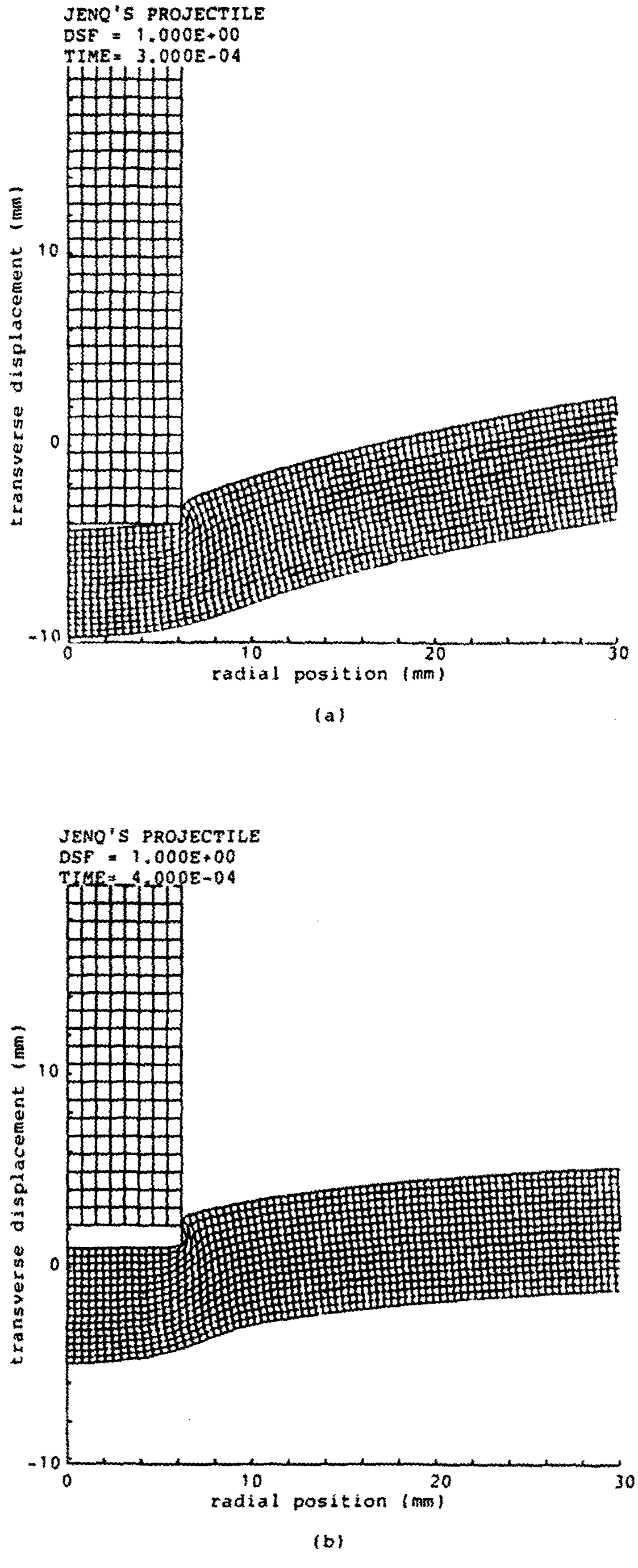

Fig. 11. Deformation vs radial position for Dyna2d plots: (a) Run D1 at time = 300 μs; (b) Run D2 at time = 400 μs.

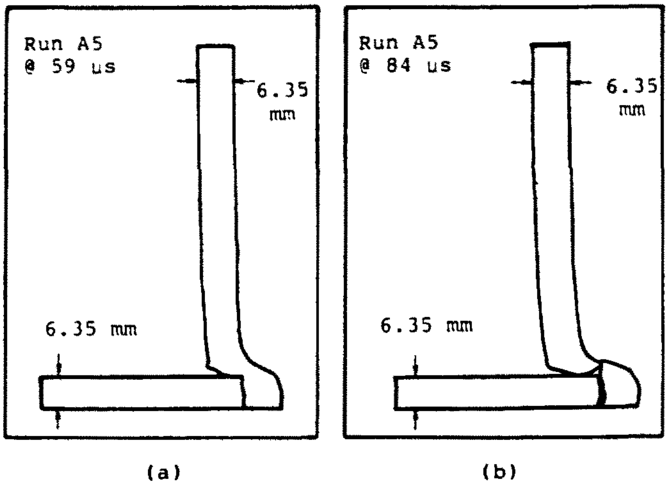

Fig. 12. Simulation of a 6.35 mm soft aluminum target struck by a 12.7 mm diameter hard-steel projectile with $v_i = 150$ m s^{-1}: (a) at 59 μs and (b) at 84 μs after impact (Run A5).

velocity obtained from the test is 110 m s^{-1}. The difference is less than 10%. Run A5 involves the non-perforated case, and the corresponding deformation profiles are plotted in Figs 14(a) and (b) at 200 and 352 μs, respectively. Figure 15 reveals that the target is stopped and rebounds.

Two similar runs, Runs A1 and A3, were also performed for a 3.18 mm thick target struck at velocities of 77 and 150 m s^{-1}, respectively. Run A3 results in target perforation whereas Run A1 does not. Figures 16 and 17 show the deformed profile for Runs A3 and A1, respectively. The maximum target deflections obtained are 14.9 and 17.3 mm for these two runs. The exit velocity for Run A3 is within 3% of the experimental data. The results obtained from the code overestimate the target deformation, especially for the non-perforated cases because the static material strength was used. The fracture processes and the material properties after damage are not precisely known for the penetration phenomenon. The artificial slide line introduced for perforated cases is based on test information. The results are satisfactory for the current runs. The codes are based on a continuum mechanics formulation; therefore, higher order effects such as the transverse shear correction are considered. The available phenomenological plugging models, such as the five-stage model of Liss *et al.* (1983a) assume that the material properties are invariant

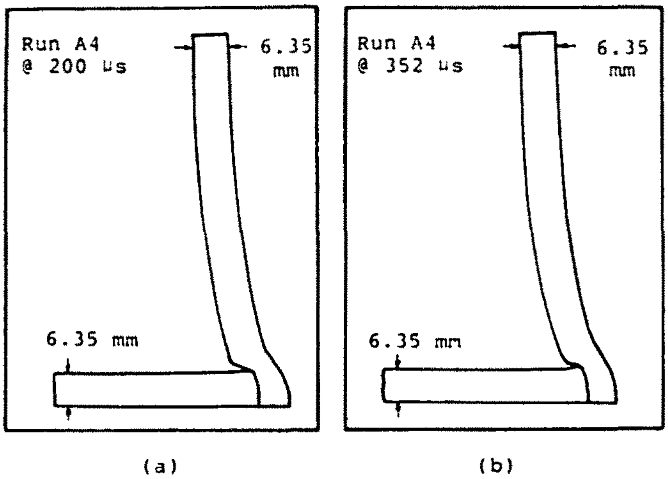

Fig. 14. Simulation of 6.35 mm target struck by a projectile with $v_i = 104$ m s^{-1}: (a) at 200 μs and (b) at 352 μs after impact (Run A4).

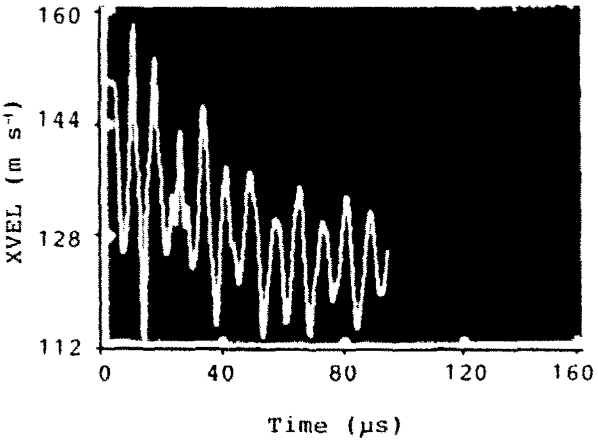

Fig. 13. Projectile particle velocity vs penetration time for Run A5.

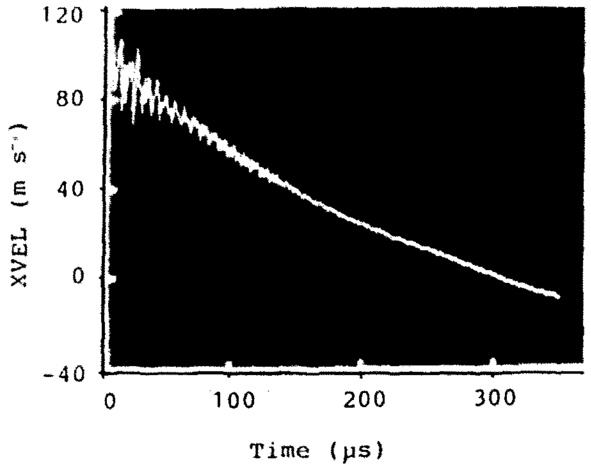

Fig. 15. Projectile particle velocity vs penetration time for Run A4.

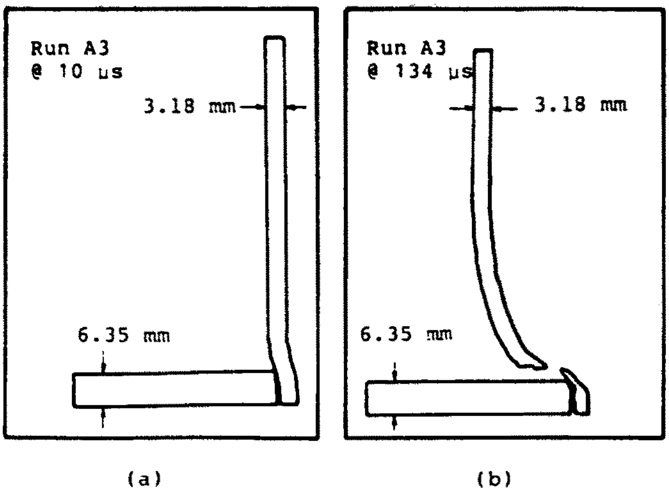

Fig. 16. Simulation of 3.18 mm aluminum target struck by a 12.7 mm diameter steel projectile with an initial velocity of 150 m s^{-1}: (a) at 10 μs and (b) at 134 μs after impact (Run A3).

during the penetration process and the perforation criterion is based on simple geometrical relations. These assumptions need to be justified. It is suggested that the material constitutive modelling and the failure criterion for the penetration should be investigated more intensively in future research.

CONCLUSIONS

The present work involved a combined phenomenological, numerical and experimental investigation designed to determine the effects of bending on the response of thin metallic targets by normal impact of rigid, blunt projectiles at velocities in the vicinity of the ballistic limit. The physical model consisted of a combination of a dynamic representation of the bending of a rigid/perfectly plastic plate with a previously developed five-stage plugging analysis. Two numerical programs, Dyna2d executed on a Cray computer, and Autodyn used on a PC, which allows generation of slide zones during the perforation process were utilized. Experimental results were obtained from normal impacts of 34 g hard-steel projectiles against soft aluminum targets with thicknesses ranging from 3.18 to 6.35 mm at

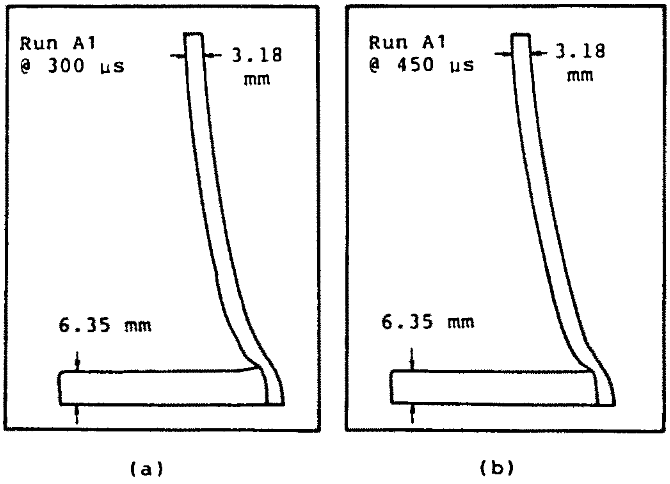

Fig. 17. Simulation of 3.18 mm thick soft aluminum target struck by a 12.7 mm diameter steel projectile with an initial velocity of 77 m s^{-1}: (a) at 300 μs and (b) at 450 μs after impact (Run A1).

velocities up to 183 m s^{-1}. Bending and shearing contributions were derived from the total slope of the plate and measurements of the angle of a pin extending from small pre-drilled holes in the samples.

It is concluded that a theory featuring bending in conjunction with a plugging model provides more accurate results than an analysis based on plate shear in the vicinity of the ballistic limit when the plates are thin compared to the projectile radius. For thicker plates, the bending and shear contributions to the central deformation are about equal. The Lagrangian finite element code Dyna2d exhibits closer correlation with experimental results when dynamic material properties are employed. The Lagrangian finite difference program Autodyn overestimate the target deflection, particularly in the absence of perforation, since static values of the material strength were employed.

Acknowledgement—This paper is based upon a dissertation submitted in partial fulfillment of the requirements of the Ph.D. degree at the University of California, Berkeley. The work was sponsored by the Army Research Office under Contract No. DAA 29-84-0021 and in part by a gift from FMC Corporation.

REFERENCES

Backman, M. and Goldsmith, W. (1978). The mechanics of penetration of projectiles into targets. *Int. J. Engng Sci.* **16**, 1–99.

Beynet, P. and Plunkett, R. (1971). Plate impact and plastic deformation by projectiles. *Expl Mech.* **11**, 64–70.

Calder, C. A. and Goldsmith, W. (1971). Plastic deformation and perforation of thin plates resulting from projectile impact. *Int. J. Solids Structures* **7**, 863–881.

Hallquist, J. O. (1978). Dyna 2D—an explicit finite element and finite difference code for axisymmetric and plane strain calculations, User's Guide. University of California, Lawrence Livermore National Laboratory, Rept. UCRL-52429.

Hauser, F. E. (1966). Techniques for measuring stress–strain relations at high strain rates. *Expl Mech.* **6**, 395–402.

Landkof, B. and Goldsmith, W. (1985). Petalling of thin metallic plates during penetration by cylindro-conical projectiles. *Int. J. Solids Structures* **21**, 245–266.

Liss, J. and Goldsmith, W. (1984). Plate perforation phenomena due to normal impact by blunt cylinders. *Int. J. Impact Engng* **2**, 37–64.

Liss, J., Goldsmith, W. and Kelly, J. M. (1983a). A phenomenological penetration model of plates. *Int. J. Impact Engng* **1**, 321–341.

Liss, J., Goldsmith, W. and Hauser, F. E. (1983b). Constraint to side flow in plates. *J. Appl. Mech.* **59**, 694–698.

Mindlin, R. D. (1951). Influence of rotatory inertia and shear on flexural motions of isotropic elastic plates. *J. Appl. Mech.* **18**, 31–38.

Ravid, M. and Bodner, S. R. (1983). Dynamic perforation of viscoplastic plates by rigid projectiles. *Int. J. Engng Sci.* **21**, 577–591.

Recht, R. F. and Ipson, T. W. (1963). Ballistic perforation dynamics. *J. Appl. Mech. E* **30**, 384–390.

Shadbolt, P. J., Corran, R. S. and Ruiz, C. (1983). A comparison of plate perforation models in the sub-ordnance impact velocity range. *Int. J. Impact Engng* **1**, 23–49.

Shawa, O. M. (1978). The application of dynamic plastic analysis to problems of structural impact. Ph.D. Dissertation, University of California, Berkeley.

Uflyand, Y. S. (1948). The propagation of waves in the transverse vibrations of bars and plates (in Russian). *Prikl. Mat. Mekh.* **12**, 287.

Valathur, M. and Baker, W. E. (1971). Wave propagation resulting from very high impact velocity. *J. Appl. Mech.* **39**, 555–557.

Woodward, R. L. (1987). A structural model for thin plate perforation by normal impact of blunt projectiles. *Int. J. Impact Engng* **5**, 129–140.